Letter

Giant Photonic Response of Mexican-Hat Topological Semiconductors for Mid-infrared to Terahertz Applications

Haowei Xu, Jian Zhou, Hua Wang, and Ju Li*

Read Online

ACCESS | Metrics & More | Article Recommendations | SI Supporting Information

ABSTRACT: The mid-infrared (MIR), far-infrared (FIR), and terahertz (THz) frequencies are the least developed parts of the electromagnetic spectrum for applications. Traditional semiconductor technologies like laser diodes and photodetectors are successful in the visible light range but are still confronted with great challenges when extended into the MIR/FIR/THz range. In this paper, we demonstrate that topological insulators (TIs), especially those with Mexican-hat band structure (MHBS), provide a route for overcoming these challenges. The optical responses of MHBS TIs can be 1−2 orders of magnitude larger than that of normal semiconductors at the optical transition edge. We explore the databases of topological materials and discover a number of MHBS TIs whose bandgaps lie between 0.05 and 0.5 eV and possess giant gains (absorption coefficients) on the order of 10^4–10^5 cm^{-1} at the transition edge. These findings may significantly boost potential MIR/FIR/THz applications such as photon sources, detectors, ultrafast electro-optical devices, and quantum information technologies.
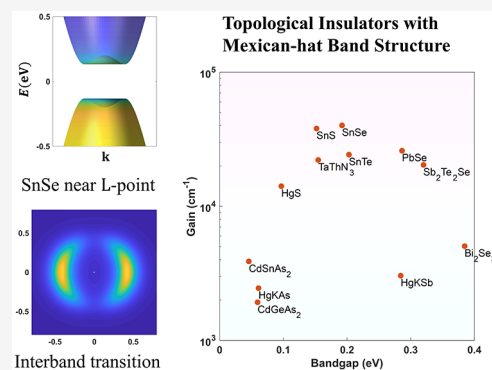
The mid-infrared (MIR), far-infrared (FIR), and terahertz (THz) frequencies are of significant importance for applications such as nondestructive inspection, communication, astrophysics, etc. However, lying between the microwave and visible frequencies of the electromagnetic spectrum, the MIR/FIR/THz frequency range is not yet sufficiently developed for many applications, limited by both photon generation and detection technologies. For photon generation, quantum cascade lasers (QCLs)[1−3] that rely on the intersubband transition of electrons in quantum wells have become the leading coherent MIR radiation source. However, when QCLs are extended to the MIR/FIR/THz range, there are still great challenges such as the physical limitations on the standard techniques of injecting electrons into the high-energy levels of the quantum well. Other mechanisms for MIR/FIR/THz generation are also being actively studied.[4−10] On the photon detection side,[11,12] a variety of physical mechanisms can be utilized, including the thermal effect of MIR/FIR/THz radiation in, e.g., a Golay cell, or the interaction between MIR/FIR/THz photons and electrons in, e.g., a Schottky barrier diode. These detectors have their pros and cons and are suitable for different applications. In general, detectors with a small noise-equivalent power and a large modulation frequency are desirable. Single THz photon detectors are also necessary for certain applications.[13,14]

In the visible range, the semiconductor laser diodes and photodetectors are widely used. They utilize the same mechanism of continuum-to-continuum (C2C) transition of an electron between the valence band (VB) and the conduction band (CB), and photon generation and detection

can be regarded as reciprocal processes, sharing the same prefactor in Fermi's golden rule. However, in the MIR/FIR/THz range, attention on semiconductor devices is mostly focused on the transition between bound-to-continuum (B2C) and bound-to-bound (B2B) states, in, e.g., an extrinsically doped semiconductor or a quantum well. Such B2C and B2B transitions impose stringent requirements on material fabrications, such as precise control on the impurity type and concentration. A C2C transition actually has huge advantages over a B2C or B2B transition. For example, the carrier mobilities would not be curtailed by dopants, and the detector may be utilized under arbitrary polarizations. However, 1 THz is equivalent to 4.1 meV, far below the typical interband gaps of most known semiconductors (on the order of 1 eV). Another significant bottleneck is that the optical transition rate decreases drastically with a decrease in photon frequency. In free space, the dipole radiation power scales as ω^4, where ω is the angular frequency of the photon. Even if an optical cavity is used to modify the photon density of states, the radiation power still scales at least with ω; thus, for a small ω, the photon emission or absorption would be slow. A third obstacle is the fact that when the bandgap of the semiconductor is
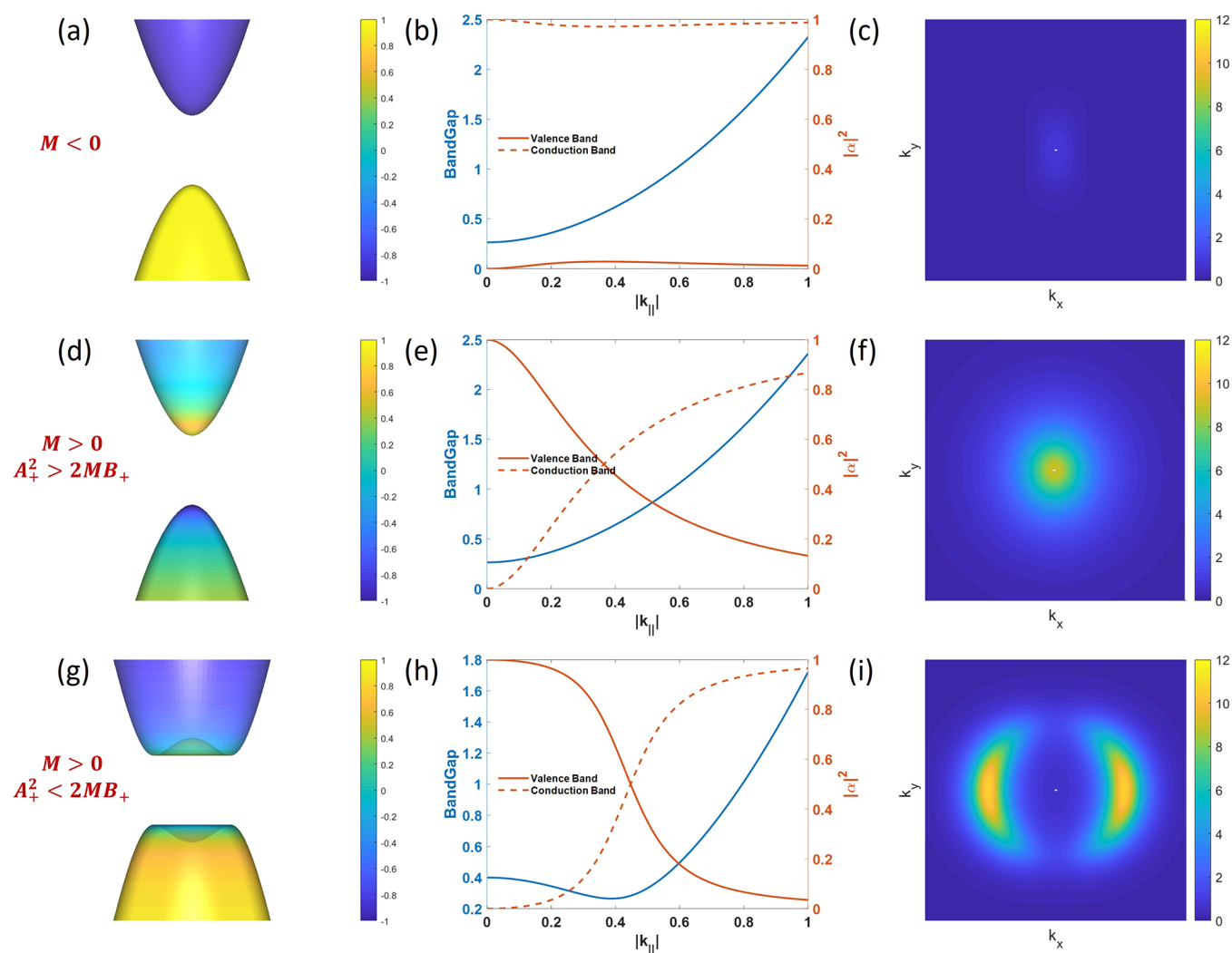
Figure 1. Band characteristics of the two-band model in eq 2. The first column shows the band dispersion in the k_x-k_y plane. The color map shows $|\alpha|^2 - |\beta|^2$, which is the difference between the contributions from two basis wave functions. The second column shows the bandgap and $|\alpha_{VB,CB}|^2$ along the radial direction of the k_x-k_y plane. The third row shows the interband mixing $O^{xx}(\mathbf{k})$ on the k_x-k_y plane. The first row corresponds to a normal insulator without band inversion, while the second and third rows correspond to topological insulators with band inversions. In particular, the third row exhibits MHBS.

below the frequency of optical phonons (usually on the order of 1−10 THz), the electron−phonon coupling will induce a rapid nonradiative interband transition, which is a dominant source of noise and loss, especially at high temperatures. Of course, the nonradiative transition via phonon coupling can be kept slow as long as the bandgap is above the optical phonon frequencies. In fact, the low optical transition rate and nonradiative transition via phonon coupling are two generic problems in all MIR/FIR/THz technologies and are not specific to the C2C transition.

In this work, we propose that topological insulators[15] (TIs)[16−18] could provide opportunities for resolving these issues. The bandgaps of many TIs fall within the MIR/FIR/THz range, and as we will show in the following, the optical responses of TIs can be significantly stronger than that of normal insulators (NIs) due to enhanced Berry connections. Provided with a Mexican-hat band structure (MHBS), the optical responses would be further boosted due to the larger joint density of states (jDOS). Consequently, the optical responses of MHBS TIs in the MIR/FIR/THz range can be 1 or 2 orders of magnitude larger than that of the widely used

MCT (HgCdTe) alloy. During the past decade, TIs have been intensely studied and have changed our understanding on the state of matter. Many novel properties of TIs such as symmetry-protected edge states could find potential applications in electronic and spintronic devices,[19,20] fault-tolerant quantum computers,[21,22] etc. From a band structure point of view, the nontrivial band topology of TIs usually comes from the inversion of energy bands with respect to their natural energy order.[18,23−25] For example, the metal d orbitals usually constitute bands with energies higher than those of the chalcogen p orbitals. However, in some materials, the metal d band could move below the chalcogen p band for some range of the wavevector $\mathbf{k}$. In this case, the metal d band would become a valence band rather than a conduction band[25] and would cause band crossings. A bandgap is opened at the band crossings under spin−orbit coupling (SOC), which alters the original space-group to a double group in spin-wavefunction space. The SOC-induced bandgap in TIs provides several advantages. First, the bandgap is usually direct, which could enable fast and efficient optical transitions and eliminate inefficient phonon coupling required for indirect bandgap

transitions. Second, the bandgap E_g is determined by the strength of SOC and is usually on the order of ≤ 0.1 eV, lying in the MIR/FIR/THz range. Furthermore, the bandgap can be controllably and continuously tuned by external field parameters ($\{\lambda_i\}$) such as strain,[26−28] composition,[29−31] or electric field.[25,32,33] In particular, varying $\{\lambda_i\}$ can trigger topological phase transitions between topologically nontrivial and trivial phases. At some critical points $\{\lambda_i^c\}$, the system would be gapless.[34−37] Consequently, arbitrarily small bandgaps can be realized around $\{\lambda_i^c\}$. In fact, the alloy widely used for infrared detection, $Hg_xCd_{1-x}Te$, takes advantage of the band inversion, as well.[38,39] The system has an inverted bandgap when $x = 1$ and a normal bandgap when $x = 0$. Between those bandgaps, a zero bandgap can be achieved by tuning the composition x.

Striking advantages of using TIs for MIR/FIR/THz applications can be revealed when considering the optical properties of bulk optical transitions in TIs. In fact, the optical response of TIs at the transition edge ($\hbar\omega = E_g$) can be 1 or 2 orders of magnitude larger than that of NIs. To illustrate this point, here we study an important parameter for optical applications, the gain $G(\omega)$ in the laser mode or, equivalently, the absorption coefficient $\mu(\omega)$ in the detector mode. $G(\omega)$ can be related to the dielectric response function $\epsilon(\omega)$ of the semiconductor by $\mu(\omega) = G(\omega) = \frac{2\omega \mathrm{Im}[\sqrt{\epsilon(\omega)}]}{c}$. The dielectric response function within the random phase approximation (RPA)[40] can be expressed as

$$\epsilon_{ij}(\omega) = \delta_{ij} - \frac{e^2}{\epsilon_0} \int \frac{d^3\mathbf{k}}{(2\pi)^3} \sum_{c,v} \frac{\langle u_{v,\mathbf{k}} | \nabla_{k_i} | u_{c,\mathbf{k}} \rangle \langle u_{c,\mathbf{k}} | \nabla_{k_j} | u_{v,\mathbf{k}} \rangle}{E_{c,\mathbf{k}} - E_{v,\mathbf{k}} - \hbar\omega - i\xi}$$

(1)

where $|u_{n,\mathbf{k}}\rangle$ and $E_{n,\mathbf{k}}$ are the periodic part of the wave function and the energy eigenvalue at band n and wavevector $\mathbf{k}$, respectively, c and v denote the CB and VB, respectively, δ_{ij} is the Kronecker delta, $i, j = x, y, z$ are Cartesian indices, and ϵ_0 is the vacuum permittivity. Close to the transition edge, only the lowest CB and highest VB need to be considered. From eq 1, one can see that two factors have a significant influence on $\epsilon(\omega)$. First, the product $O^{ij}(\mathbf{k}) \equiv |A_{cv}^i(\mathbf{k}) A_{vc}^j(\mathbf{k})|$, where $\mathbf{A}_{mn}(\mathbf{k}) \equiv i\langle u_{m,\mathbf{k}} | \nabla_{\mathbf{k}} | u_{n,\mathbf{k}} \rangle$ is the Berry connection. To have a large Berry connection, the wave functions of CB and VB should have large extents of mixing. The second factor is the joint density of states (jDOS), $\rho_{cv}(\omega)$, which comes into play via the Brillouin zone (BZ) integration. In principle, both $O(\mathbf{k})$ and $\rho_{cv}(\omega)$ are determined by the band characteristics, including the energy dispersion and the orbital contributions in each band. The details of the band characteristics are dependent on the material, but the essence of band inversion, a telltale feature of TIs, can be understood with the help of a two-band model Hamiltonian.[23,24,41] The basis wave functions are denoted as $|\psi_1\rangle$ and $|\psi_2\rangle$, which are usually orthogonal and have a small extents of mixing. The Hamiltonian can be written as

$$H(\mathbf{k}) = \begin{bmatrix} M - B_+|k_+|^2 - B_z k_z^2 & A_+ k_+ + A_z k_z \\ A_+ k_+^* + A_z k_z & -(M - B_+|k_+|^2 - B_z k_z^2) \end{bmatrix}$$

(2)

Here we assume some basic crystal symmetries (e.g., in-plane 3-fold or 4-fold rotational symmetry) so that the mixing terms for in-plane wavevectors $k_{x,y}$ are identical and are denoted by

A_+ and B_+. $k_+ \equiv k_x + ik_y$ is the in-plane complex momentum. M characterizes the band inversion. By solving eq 2, one obtains the band dispersion

$$E_{\pm}(\mathbf{k}) = \pm\sqrt{(M - B_+|k_+|^2 - B_z k_z^2)^2 + |A_+ k_+ + A_z k_z|^2}$$

(3)

The wave functions are $|VB\rangle = \alpha_{VB}(\mathbf{k})|\psi_1\rangle + \beta_{VB}(\mathbf{k})|\psi_2\rangle$ and $|CB\rangle = \alpha_{CB}(\mathbf{k})|\psi_1\rangle + \beta_{CB}(\mathbf{k})|\psi_2\rangle$.

Without a loss of generality, we set $k_z = 0$ and focus on the $k_x - k_y$ plane. Some band characteristics on the $k_x - k_y$ plane are plotted in Figure 1. The three columns are $E(\mathbf{k})$, $|\alpha_{VB,CB}(\mathbf{k})|^2$, and $O^{xx}(\mathbf{k})$. Panels a−c correspond to $M < 0$, while the second (panels d−f) and third (panels g−i) rows have $M > 0$. For all three rows, the parameters are adjusted so that the direct bandgaps are identical. When M is negative, the mass term $M - B_+|k_+|^2 < 0$, and the VB and CB are dominantly composed of $|\psi_2\rangle$ and $|\psi_1\rangle$ for all values of k_+ (Figure 1b). There is no band inversion, corresponding to a topologically trivial state. $O^{xx}(\mathbf{k})$ in this case is plotted in Figure 1c, where we can see that it is quite small. On the other hand, when M is positive, band inversion occurs, and the band dispersion has different shapes depending on the magnitude of M, A_+, and B_+ (Figure 1d,g). When $A_+^2 > 2MB_+$ (Figure 1d−f), the band dispersion is nearly parabolic, with the band edge lying at $\mathbf{k} = 0$. When $A_+^2 < 2MB_+$ (Figure 1g−i), the band dispersion shows MHBS, with the band edge forming a ring at finite $|k_+|$. The wave function compositions undergo an inversion for both cases. At a small $|k_+|$, the mass term is positive and the VB and CB are dominated by ψ_1 and ψ_2, respectively. On the other hand, when $|k_+|$ is large, the mass term becomes negative and the orbital contributions to the two bands are inverted, with the VB and CB dominated by $|\psi_2\rangle$ and $|\psi_1\rangle$, respectively. Such a band inversion usually indicates a nontrivial band topology. Between these two extremes, the VB and CB have comparable contributions from both $|\psi_1\rangle$ and $|\psi_2\rangle$. Because of the band inversion, $\nabla_{\mathbf{k}}\alpha(\mathbf{k})$ and $\nabla_{\mathbf{k}}\beta(\mathbf{k})$ are larger than those in the topologically trivial case, and the wave function overlap is also stronger. Consequently, $O(\mathbf{k})$ is supposed to be larger, which is verified by the numerical results in panels f and i of Figure 1, where we can see that the maximum value of $O(\mathbf{k})$ and its $\mathbf{k}$-space distribution are much larger than that in Figure 1c. Note that $O(\mathbf{k})$ does not appear to be isotropic in panels c, f, and i of Figure 1 because only $O^{xx}(\mathbf{k})$ is plotted; the isotropy would be restored when the $O^{yy}(\mathbf{k})$ contribution is added.

As stated above, the band inversion alone can contribute to a stronger and faster interband transition. This would already lead to stronger optical responses for both parabolic and MHBS TIs (see the Supporting Information). However, the MHBS provides an additional and even more striking advantage: a greater jDOS at the transition edge. The jDOS can be written as

$$\rho_{cv}(\omega) = \frac{2}{(2\pi)^d} \int_{E_c - E_v = \hbar\omega} \frac{dS}{|\nabla_{\mathbf{k}}(E_c - E_v)|}$$

(4)

where d is the dimensionality of the system and the integration is over the constant energy difference surface (CEDS) with $E_c - E_v = \hbar\omega$ in the first BZ. For a standard parabolic band structure, it is well-known that in three dimensions, $\rho_{cv}(\omega)$ scales as $\sqrt{\hbar\omega - E_g}$ and is zero at the transition edge. On the contrary, in two dimensions, $\rho_{cv}(\omega)$ should be a constant. However, with MHBS as in eq 3, it can be shown that at the transition edge, $\rho_{cv}(E_g)$ is a finite value in three dimensions and
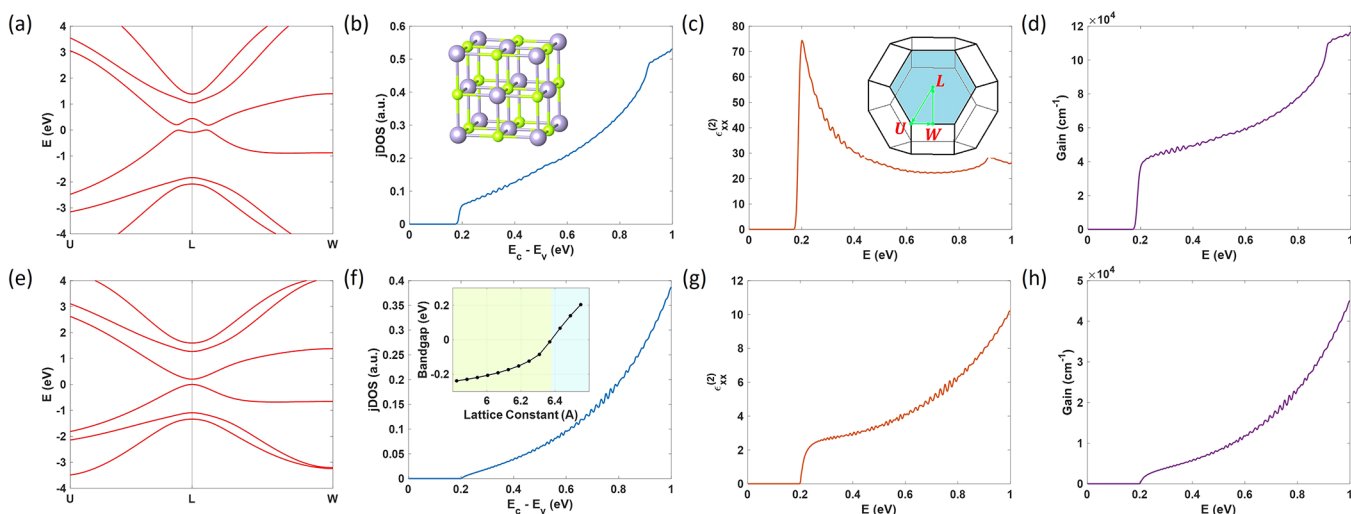
Figure 2. Band structure and optical properties of cubic SnSe. The four columns correspond to the band structure, jDOS, imaginary part of the dielectric function, and gain, respectively. For the first row (a−d), the atomic structure of SnSe is fully relaxed, and it is a topological crystalline insulator (TCI) with MHBS. The second row (e−h) corresponds to SnSe under an 8% triaxial strain, which is normal insulating without band inversion. The dramatic improvement in the optical properties by the band inversion and MHBS can be seen by comparing two rows. The inset of panel b shows the atomic structure of cubic SnSe. The inset of panel c shows the first BZ of cubic SnSe. The band edge is on the L point, and the MHBS is on the cyan hexagonal surface. The inset of panel f shows the bandgap of cubic SnSe as a function of lattice constant a. When $a \lesssim 6.4$ Å, SnSe is a TCI with an inverted bandgap. When $a \gtrsim 6.4$ Å, it is a normal insulator. A negative bandgap indicates that it is an inverted bandgap.

is infinite in two dimensions. This can be understood by a geometric analysis. For a parabolic band structure, the CEDS is a zero-dimensional point at the transition edge, whereas for MHBS, the CEDS forms a one-dimensional closed loop, which boosts $\rho_{cv}(E_g)$ from zero to a finite value in three dimensions and from a finite value to infinity in two dimensions. Consequently, in three dimensions, the gain $G(\omega)$ would abruptly jump to a finite value, rather than starting from zero and increasing smoothly at the transition edge, while in two dimensions, the gain would exhibit a sharp peak at the transition edge (see the Supporting Information).

We take three-dimensional (3D) cubic SnSe (space group $Fm\overline{3}m$) as an example to illustrate our theory. The atomic structure of SnSe is shown in the inset of Figure 2b. Previous studies have demonstrated that SnSe is a topological crystalline insulator (TCI)[42,43] with fully relaxed lattice constants $a = b = c = 6.07$ Å. Here the band structure, band topology, and optical properties are calculated with density functional theory (DFT) with the Perdew−Burke−Ernzerhof (PBE)[44] functional. Results with the Heyd, Scuseria, and Ernzerhof (HSE)[45,46] hybrid functional can be found in the Supporting Information. The band structure is shown in Figure 2a, where the fundamental bandgap at the L point is inverted with a magnitude of −0.53 eV. Then the SOC opens an inverted bandgap E_g of 0.21 eV around the L point. The first BZ of cubic SnSe is a truncated octahedron (inset of Figure 2c), and the L point is the center of the hexagonal (111) faces (colored cyan). On the hexagonal face, the system has a 3-fold rotational symmetry. Therefore, the Hamiltonian in eq 2 can be applied here. The k_x−k_y plane is on the hexagonal surface, while z is along the Γ−L direction. As expected, the inverted bandgap forms a ring on the hexagonal face, and the jDOS abruptly jumps to a finite value at the transition edge (Figure 2b). The imaginary part of the dielectric function $\epsilon_{xx}^{(2)}(\omega)$ is plotted in Figure 2c. There is a strong peak around E_g, which is rarely seen in the dielectric response of normal 3D insulators. As discussed above, the peak should be attributed to (1) strong

VB and CB wave function mixing due to band inversion and (2) a large jDOS around E_g owing to the MHBS. Finally, the gain $G(\omega)$ (Figure 1d) jumps to a tremendous value of 4×10^4 cm^{-1} at an E_g of ∼0.2 eV, which is comparable in magnitude to that of GaAs in the visible light range.[47]

To fully compare the salient merits of the MHBS topological materials with that of NIs, we elastically strained the lattice parameter of SnSe while keeping its cubic phase, so that it undergoes a topological phase transition and becomes a NI. The bandgap variation as a function of strain is shown in the inset of Figure 2f. The phase transition happens around $a = 6.4$ Å. When the lattice constant $a \lesssim 6.4$ Å, SnSe remains topologically nontrivial, whereas when $a \gtrsim 6.4$ Å, the inverted bandgap disappears and SnSe becomes a NI. Furthermore, when $a = 6.55$ Å (corresponding to an 8% tensile strain), the normal bandgap is also 0.2 eV, close to the inverted bandgap in the strain-free state. Thus, we calculate the optical properties of SnSe with $a = 6.55$ Å. The results (Figure 2e−h) exhibit typical features of a NI. The jDOS, dielectric response, and gain all slowly increase from zero at E_g. Even at 0.3 eV, the gain is still only 4×10^3 cm^{-1}, 10 times smaller than that in the strain-free topological case at $E_g = 0.2$ eV (Figure 2d). This demonstrates that the optical response and its potential applications (such as the laser mode gain and detector mode absorption) can be greatly enhanced in topological materials (TI or TCI) with MHBS by 1 or 2 orders of magnitude. Therefore, thin-film photonic devices made with such Mexican-hat TIs can be much thinner than those made with normal semiconductors, while maintaining a high photon detection efficiency and/or emissivity.

Finally, to search for more topological materials for MIR/FIR/THz applications, we explored the entire databases of topological material[48,49] and calculated the optical properties of TIs with MHBS. One should note that the database is constructed with the PBE functional and would be different if an HSE functional were used. Here we focus on the PBE database for the present illustrative work. We first mapped out

Table 1. Materials in Figure 3d[a]

material	ICSD	space group	lattice constant (Å)	bandgap (eV)	gain ($\times10^3$ cm^{-1})
Bi_2Se_3	617072	166 ($R\bar{3}m$)	$a = b = 4.39$, $c = 30.50$	0.385	5.04
Sb_2Te_2Se	2085	166 ($R\bar{3}m$)	$a = b = 4.19$, $c = 29.94$	0.320	20.4
$CdGeAs_2$	16736	122 ($I\bar{4}2d$)	$a = b = 5.94$, $c = 11.22$	0.059	1.92
$CdSnAs_2$	16737	122 ($I\bar{4}2d$)	$a = b = 6.09$, $c = 11.92$	0.046	3.88
HgKSb	56201	194 ($P6_3/mmc$)	$a = b = 4.78$, $c = 10.23$	0.284	3.04
HgKAs	10458	194 ($P6_3/mmc$)	$a = b = 4.51$, $c = 9.98$	0.061	2.45
HgS	56476	216 ($F\bar{4}3m$)	$a = b = c = 5.85$	0.097	14.1
PbSe	238502	225 ($Fm\bar{3}m$)	$a = b = c = 6.01$	0.286	26.0
SnS	651015	225 ($Fm\bar{3}m$)	$a = b = c = 5.80$	0.152	38.0
SnSe	52424	225 ($Fm\bar{3}m$)	$a = b = c = 5.99$	0.192	40.1
SnTe	52489	225 ($Fm\bar{3}m$)	$a = b = c = 6.32$	0.203	24.3
$TaThN_3$	77661	221 ($Pm\bar{3}m$)	$a = b = c = 4.02$	0.155	22.2

[a]The results are from DFT calculations with the PBE functional. The band topology of these materials with the HSE hybrid functional can be found in the Supporting Information.
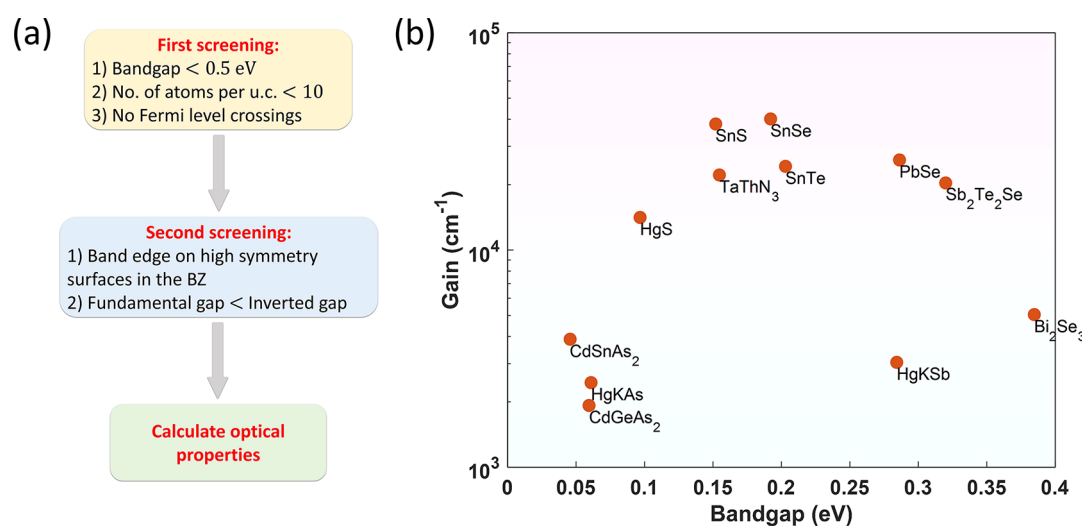

Figure 3. (a) Workflow for exploring materials with enhanced optical properties in the MIR/FIR/THz range in the topological material database. (b) Scattering plot of the bandgap and gain of materials targeted by the workflow in panel a.

TIs with a bandgap below 0.5 eV ($\approx$120 THz), with fewer than 10 atoms per unit cell, and without any Fermi level crossings. Then we carried out a screening by investigating the crystalline symmetry and band structures of these TIs and targeted candidates that could potentially have MHBS over at least one surface in the BZ. Finally, we calculated the optical properties of these candidate TIs. The results are plotted in Figure 3b (see also Table 1), where we can see a number of TIs with $G(\omega)$ over 10^4 cm^{-1} at the transition edge ranging from 0.1 to 0.5 eV. There are also three TIs (HgKAs, CdSnAs$_2$, and CdGeAs$_2$) whose bandgaps are around 0.05 eV and $G(E_g)$ values are on the order of several 10^3 cm^{-1}. To eliminate possible photon–phonon transitions, materials with bandgaps that are too small (<10 THz) are not considered here. Note that because the optical transition rate is slower for a small ω, it is harder to obtain a large $G(\omega)$ at a small ω {also manifested by the relation $G(\omega) = \frac{2\omega\text{Im}[\sqrt{\epsilon(\omega)}]}{c}$}. These TIs should be compared with the widely used infrared detector, Hg$_x$Cd$_{1-x}$Te (MCT) alloy. The gain/absorption coefficient of Hg$_x$Cd$_{1-x}$Te is only around 10^3 cm^{-1} near the transition edge.[50] In other words, the performance of the TIs as listed in Figure 3b is at least 10 times better than that of Hg$_x$Cd$_{1-x}$Te in terms of the

gain/absorption coefficient and should be of primary technological interest.

Before concluding, we make several remarks. First, the enhancement of the optical response in Mexican-hat TIs is a bulk effect, rather than surface effects that have been widely studied in TIs. Thus, the enhancement of optical responses in TIs with MHBS can be applied to two-dimensional (2D) materials, as well, which have bulk interaction with light. As discussed before, in addition to the large interband Berry connection, the jDOS of 2D Mexican-hat materials can be infinity at the transition edge. As a result, the absorbance of 2D Mexican-hat TIs can be dramatically improved, which is verified with a 2D monolayer SnF[51] as shown in the Supporting Information. Furthermore, quantum wells constructed with 3D materials are effectively 2D materials due to the confinement in the z direction; thus, they should exhibit similar properties, as well, which is advantageous for applications like laser diodes.

Second, the 2D surfaces of 3D TIs are semimetallic with a vanishing bandgap. Therefore, they could affect the performance of TIs as light sources or detectors by providing a route for nonradiative recombination of electrons and holes in the laser mode, or by reflecting the incoming light in the detector mode. However, these effects should be relatively weak

compared to the bulk effect in the frequency range of interest for the following reasons. First, the surface states are actually semimetallic, meaning that the free carrier concentration on the surface is low. In practice, there could be free carriers from, e.g., doping or thermal activation, but the density of these free carriers n should be smaller by several orders of magnitude than that in real metals such as copper, the value of which is on the order of 10^{28} m^{-3}. Assuming the surface free carrier concentration n is 10^{23} m^{-3} within the penetration depth (~1 nm) of the surface states, the free carrier contribution to the dielectric function of SnSe is only on the order of 100 even at ω = 1 THz from Drude model (see the Supporting Information), which is smaller than that of copper by 5 orders of magnitude. Because the interband contribution is also ~100, the total dielectric function of the surface states is on the order of 100 within the ~1 nm skin depth, which is not so large. Therefore, the absorption and reflection from surface states are much less efficient than in real metals. Also, when $n = 10^{23}$ m^{-2}, the surface carrier plasmon frequency is ~2 THz ~ 8 meV, well below the bandgap of the bulk material, which is the frequency region of interest. Second, the surface states exist only near the surface with a small (joint) DOS. The thickness of these surface states is on the order of 1 nm, which is much smaller than the wavelength of MIR/FIR/THz photons and the size of typical bulk materials. In the detector mode, the surface states might reflect the incoming light. However, to obtain full reflection, the penetration depth of light upon reflection needs to be comparable with its wavelength, which is on the order of 0.1–1 μm with $\epsilon \approx 100$. This is much larger than the thickness of the surface states. Therefore, these surfaces states are too thin to reflect the incoming light strongly, and thus, light can penetrate into the bulk. For example, monolayer graphene, despite being a Dirac metal, allows 97.4% light transmission. Actually, experimental works have shown that the total reflectivity of several TIs is ~0.5 near the bulk bandgap.[52−54] Considering that the total reflectivity includes the contribution from the bulk, the reflectivity contribution from surface electronic states should be less significant. In the laser mode, the bulk states are extended over the entire bulk. By a simple size analysis, one can see that the (joint) DOS of the bulk states is much larger than that of the surface states, the thickness of which is only ~1 nm. Therefore, the nonradiative recombination on the surfaces should be weak compared with the radiative recombination in the bulk due to the small (joint) DOS. Furthermore, the stimulated amplification would drastically accelerate the radiative recombination in the bulk, rendering the influence of the surface states even weaker. More detailed discussions on the influence of the surface states can be found in the Supporting Information.

Third, the optical responses of TIs in Figure 3b are boosted by the combination of two factors, namely, the large Berry connection and the large jDOS. However, each factor alone could contribute to an enhanced optical response. Therefore, a common TI with a parabolic band structure could also have an augmented optical response compared to that of NIs. In fact, with the model Hamiltonian eq 2, the imaginary part of the dielectric function $\epsilon^{(2)}$ of the TI without MHBS is ~3 times larger than that of the NI near the transition edge (see the Supporting Information), due to TI-induced band mixing (compare Figure 1e to Figure 1b). In addition, we only explored TIs in the databases of topological materials, but the band inversion does not necessarily lead to a nontrivial band topology; thus, materials outside of the topological materials database could also have inverted band structure and Mexican-hat features. Thus, many other materials with MHBS and/or band-mixing features could have an enhanced optical response that could enable efficient MIR/FIR/THz applications. The discovery and characterization of those materials shall be discussed elsewhere.

Finally, in this work, we studied only the linear optical responses. Actually, the nonlinear optical responses, such as the second-harmonic generation and bulk photovoltaic effect, could also be boosted in TIs, especially those with MHBS.

In conclusion, we have demonstrated giant continuum-to-continuum (C2C) optical responses at the conduction-to-valence interband transition edge of topological materials with MHBS. By investigating their wavefunction characteristics, we attribute the giant optical response to two factors, namely, the larger jDOS, and stronger wavefunction mixing due to band inversion. We explored the entire databases of topological materials and discovered a number of TIs with remarkable photonic responses, which could enable efficient MIR/FIR/THz photon generation, detection, and manipulation.

■ METHODS

The first-principles calculations are based on DFT[55,56] as implemented in the Vienna *ab initio* simulation package (VASP).[57,58] Generalized gradient approximation (GGA) of the Perdew−Burke−Ernzerhof (PBE)[44] form is used to treat the exchange-correlation interactions. Core and valence electrons are treated by projector-augmented wave (PAW) method[59] and a plane wave basis set, respectively. For the DFT calculations, the first Brillouin zone is sampled by a Γ-centered **k**-mesh with a grid density of at least $2\pi \times 0.02$ Å^{-1} along each dimension. The Bloch waves from DFT calculations are projected onto the maximally localized Wannier functions (MLWF) with the Wannier90 package.[60] Then a tight-binding (TB) Hamiltonian is constructed from the MLWF, and the TB Hamiltonian is used to calculate the dielectric function in eq 1 on a much denser **k**-mesh with a grid density of at least $2\pi \times 0.001$ Å^{-1} along each dimension.

■ ASSOCIATED CONTENT

ⓈI Supporting Information

The Supporting Information is available free of charge at https://pubs.acs.org/doi/10.1021/acs.jpclett.0c01552.

> Optical responses of 2D TIs with MHBS, optical responses of TIs without MHBS, influence of surface states, and results with HSE hybrid functionals (PDF)

■ AUTHOR INFORMATION

Corresponding Author

Ju Li − *Department of Nuclear Science and Engineering and Department of Materials Science and Engineering, Massachusetts Institute of Technology, Cambridge, Massachusetts 02139, United States;* ⓞ orcid.org/0000-0002-7841-8058; Email: liju@mit.edu

Authors

Haowei Xu − *Department of Nuclear Science and Engineering, Massachusetts Institute of Technology, Cambridge, Massachusetts 02139, United States*

Jian Zhou − *Department of Nuclear Science and Engineering, Massachusetts Institute of Technology, Cambridge,*

Massachusetts 02139, United States; ● orcid.org/0000-0002-2606-4833

Hua Wang − Department of Nuclear Science and Engineering, Massachusetts Institute of Technology, Cambridge, Massachusetts 02139, United States

Notes

The authors declare no competing financial interest.

■ REFERENCES

(1) Faist, J.; Capasso, F.; Sivco, D. L.; Sirtori, C.; Hutchinson, A. L.; Cho, A. Y. Quantum Cascade Laser. *Science* **1994**, *264* (5158), 553−556.

(2) Williams, B. S. Terahertz Quantum-Cascade Lasers. *Nat. Photonics* **2007**, *1* (9), 517−525.

(3) Belkin, M. A.; Capasso, F. New Frontiers in Quantum Cascade Lasers: High Performance Room Temperature Terahertz Sources. *Phys. Scr.* **2015**, *90* (11), 118002.

(4) Chang, T. Y.; Bridges, T. J. Laser Action at 452, 496, and 541 Mm in Optically Pumped CH3F. *Opt. Commun.* **1970**, *1* (9), 423−426.

(5) Wang, F.; Lee, J.; Phillips, D. J.; Holliday, S. G.; Chua, S.-L.; Bravo-Abad, J.; Joannopoulos, J. D.; Soljačić, M.; Johnson, S. G.; Everitt, H. O. A High-Efficiency Regime for Gas-Phase Terahertz Lasers. *Proc. Natl. Acad. Sci. U. S. A.* **2018**, *115* (26), 6614−6619.

(6) Schneider, C.; Rahimi-Iman, A.; Kim, N. Y.; Fischer, J.; Savenko, I. G.; Amthor, M.; Lermer, M.; Wolf, A.; Worschech, L.; Kulakovskii, V. D.; et al. An Electrically Pumped Polariton Laser. *Nature* **2013**, *497* (7449), 348−352.

(7) Bhattacharya, P.; Xiao, B.; Das, A.; Bhowmick, S.; Heo, J. Solid State Electrically Injected Exciton-Polariton Laser. *Phys. Rev. Lett.* **2013**, *110* (20), 206403.

(8) Kavokin, A. The Rise of the Bosonic Laser. *Nat. Photonics* **2013**, *7* (8), 591−592.

(9) Kavokin, K. V.; Kaliteevski, M. A.; Abram, R. A.; Kavokin, A. V.; Sharkova, S.; Shelykh, I. A. Stimulated Emission of Terahertz Radiation by Exciton-Polariton Lasers. *Appl. Phys. Lett.* **2010**, *97* (20), 201111.

(10) Liew, T. C. H.; Glazov, M. M.; Kavokin, K. V.; Shelykh, I. A.; Kaliteevski, M. A.; Kavokin, A. V. Proposal for a Bosonic Cascade Laser. *Phys. Rev. Lett.* **2013**, *110* (4), 047402.

(11) Sizov, F.; Rogalski, A. THz Detectors. *Progress in Quantum Electronics*; Pergamon, 2010; pp 278−347.

(12) Lewis, R. A. A Review of Terahertz Detectors. *J. Phys. D: Appl. Phys.* **2019**, *52* (43), 433001.

(13) Komiyama, S. Single-Photon Detectors in the Terahertz Range. *IEEE J. Sel. Top. Quantum Electron.* **2011**, *17* (1), 54−66.

(14) Echternach, P. M.; Pepper, B. J.; Reck, T.; Bradford, C. M. Single Photon Detection of 1.5 THz Radiation with the Quantum Capacitance Detector. *Nat. Astron.* **2018**, *2* (1), 90−97.

(15) The term "insulators" is widely used in the field of topological materials (TI/NI). While the materials studied in this paper should be semiconductors due to their small bandgaps, we will use *insulators* and *semiconductors* interchangeably in the following.

(16) Hasan, M. Z.; Kane, C. L. Colloquium: Topological Insulators. *Rev. Mod. Phys.* **2010**, *82* (4), 3045−3067.

(17) Qi, X. L.; Zhang, S. C. Topological Insulators and Superconductors. *Rev. Mod. Phys.* **2011**, *83* (4), 1057.

(18) Bansil, A.; Lin, H.; Das, T. Colloquium: Topological Band Theory. *Rev. Mod. Phys.* **2016**, *88* (2), 021004.

(19) Pesin, D.; MacDonald, A. H. Spintronics and Pseudospintronics in Graphene and Topological Insulators. *Nat. Mater.* **2012**, *11* (5), 409−416.

(20) Jansen, R. Silicon Spintronics. *Nat. Mater.* **2012**, *11*, 400−408.

(21) Shor, P. W. *Algorithms for Quantum Computation: Discrete Logarithms and Factoring*; Institute of Electrical and Electronics Engineers (IEEE), 2002; pp 124−134.

(22) Ladd, T. D.; Jelezko, F.; Laflamme, R.; Nakamura, Y.; Monroe, C.; O'Brien, J. L. Quantum Computers. *Nature* **2010**, *464*, 45−53.

(23) Bernevig, B. A.; Hughes, T. L.; Zhang, S. C. Quantum Spin Hall Effect and Topological Phase Transition in HgTe Quantum Wells. *Science (Washington, DC, U. S.)* **2006**, *314* (5806), 1757−1761.

(24) Zhang, H.; Liu, C. X.; Qi, X. L.; Dai, X.; Fang, Z.; Zhang, S. C. Topological Insulators in Bi 2 Se 3, Bi 2 Te 3 and Sb 2 Te 3 with a Single Dirac Cone on the Surface. *Nat. Phys.* **2009**, *5* (6), 438−442.

(25) Qian, X.; Liu, J.; Fu, L.; Li, J. Quantum Spin Hall Effect in Two - Dimensional Transition Metal Dichalcogenides. *Science (Washington, DC, U. S.)* **2014**, *346* (6215), 1344−1347.

(26) Liu, C. C.; Zhou, J. J.; Yao, Y.; Zhang, F. Weak Topological Insulators and Composite Weyl Semimetals: β-Bi4 × 4 (X = Br, I). *Phys. Rev. Lett.* **2016**, *116* (6), 066801.

(27) Aramberri, H.; Muñoz, M. C. Strain Effects in Topological Insulators: Topological Order and the Emergence of Switchable Topological Interface States in Sb2 Te3/ Bi2 Te3 Heterojunctions. *Phys. Rev. B: Condens. Matter Mater. Phys.* **2017**, *95* (20), 205422.

(28) Mutch, J.; Chen, W. C.; Went, P.; Qian, T.; Wilson, I. Z.; Andreev, A.; Chen, C. C.; Chu, J. H. Evidence for a Strain-Tuned Topological Phase Transition in ZrTe5. *Sci. Adv.* **2019**, *5* (8), No. eaav9771.

(29) Fu, L.; Kane, C. L. Topological Insulators with Inversion Symmetry. *Phys. Rev. B: Condens. Matter Mater. Phys.* **2007**, *76* (4), 045302.

(30) Hsieh, D.; Xia, Y.; Qian, D.; Wray, L.; Dil, J. H.; Meier, F.; Osterwalder, J.; Patthey, L.; Checkelsky, J. G.; Ong, N. P.; et al. A Tunable Topological Insulator in the Spin Helical Dirac Transport Regime. *Nature* **2009**, *460* (7259), 1101−1105.

(31) Sato, T.; Segawa, K.; Kosaka, K.; Souma, S.; Nakayama, K.; Eto, K.; Minami, T.; Ando, Y.; Takahashi, T. Unexpected Mass Acquisition of Dirac Fermions at the Quantum Phase Transition of a Topological Insulator. *Nat. Phys.* **2011**, *7* (11), 840−844.

(32) Kim, M.; Kim, C. H.; Kim, H. S.; Ihm, J. Topological Quantum Phase Transitions Driven by External Electric Fields in Sb 2Te 3 Thin Films. *Proc. Natl. Acad. Sci. U. S. A.* **2012**, *109* (3), 671−674.

(33) Collins, J. L.; Tadich, A.; Wu, W.; Gomes, L. C.; Rodrigues, J. N. B.; Liu, C.; Hellerstedt, J.; Ryu, H.; Tang, S.; Mo, S. K.; et al. Electric-Field-Tuned Topological Phase Transition in Ultrathin Na 3 Bi. *Nature* **2018**, *564*, 390−394.

(34) Murakami, S.; Iso, S.; Avishai, Y.; Onoda, M.; Nagaosa, N. Tuning Phase Transition between Quantum Spin Hall and Ordinary Insulating Phases. *Phys. Rev. B: Condens. Matter Mater. Phys.* **2007**, *76* (20), 205304.

(35) Murakami, S. Phase Transition between the Quantum Spin Hall and Insulator Phases in 3D: Emergence of a Topological Gapless Phase. *New J. Phys.* **2008**, *10*, 029802.

(36) Murakami, S.; Kuga, S. I. Universal Phase Diagrams for the Quantum Spin Hall Systems. *Phys. Rev. B: Condens. Matter Mater. Phys.* **2008**, *78* (16), 165313.

(37) Yang, B. J.; Nagaosa, N. Classification of Stable Three-Dimensional Dirac Semimetals with Nontrivial Topology. *Nat. Commun.* **2014**, *5* (1), 4898.

(38) Norton, P. HgCdTe Infrared Detectors. *Opto-Electron. Rev.* **2002**, *10* (3), 159−174.

(39) Nicklas, J. W.; Wilkins, J. W. Accurate Electronic Properties for (Hg,Cd)Te Systems Using Hybrid Density Functional Theory. *Phys. Rev. B: Condens. Matter Mater. Phys.* **2011**, *84* (12), 121308.

(40) Gajdoš, M.; Hummer, K.; Kresse, G.; Furthmüller, J.; Bechstedt, F. Linear Optical Properties in the Projector-Augmented Wave Methodology. *Phys. Rev. B: Condens. Matter Mater. Phys.* **2006**, *73* (4), 045112.

(41) Liu, C. X.; Qi, X. L.; Zhang, H.; Dai, X.; Fang, Z.; Zhang, S. C. Model Hamiltonian for Topological Insulators. *Phys. Rev. B: Condens. Matter Mater. Phys.* **2010**, *82* (4), 045122.

(42) Fu, L. Topological Crystalline Insulators. *Phys. Rev. Lett.* **2011**, *106* (10), 106802.

(43) Hsieh, T. H.; Lin, H.; Liu, J.; Duan, W.; Bansil, A.; Fu, L. Topological Crystalline Insulators in the SnTe Material Class. *Nat. Commun.* **2012**, *3* (1), 982.

(44) Perdew, J. P.; Burke, K.; Ernzerhof, M. Generalized Gradient Approximation Made Simple. *Phys. Rev. Lett.* **1996**, *77* (18), 3865−3868.

(45) Heyd, J.; Scuseria, G. E.; Ernzerhof, M. Hybrid Functionals Based on a Screened Coulomb Potential. *J. Chem. Phys.* **2003**, *118* (18), 8207−8215.

(46) Heyd, J.; Scuseria, G. E.; Ernzerhof, M. Erratum: "Hybrid Functionals Based on a Screened Coulomb Potential. *J. Chem. Phys.* **2003**, *118*, 8207; *J. Chem. Phys.* **2006**, *124* (21), 219906.

(47) Casey, H. C.; Sell, D. D.; Wecht, K. W. Concentration Dependence of the Absorption Coefficient for N- and p-Type GaAs between 1.3 and 1.6 EV. *J. Appl. Phys.* **1975**, *46* (1), 250−257.

(48) Bradlyn, B.; Elcoro, L.; Cano, J.; Vergniory, M. G.; Wang, Z.; Felser, C.; Aroyo, M. I.; Bernevig, B. A. Topological Quantum Chemistry. *Nature* **2017**, *547* (7663), 298−305.

(49) Vergniory, M. G.; Elcoro, L.; Felser, C.; Regnault, N.; Bernevig, B. A.; Wang, Z. A Complete Catalogue of High-Quality Topological Materials. *Nature* **2019**, *566* (7745), 480−485.

(50) Scott, M. W. Energy Gap in Hg1-XCdxTe by Optical Absorption. *J. Appl. Phys.* **1969**, *40* (10), 4077−4081.

(51) Xu, Y.; Yan, B.; Zhang, H. J.; Wang, J.; Xu, G.; Tang, P.; Duan, W.; Zhang, S. C. Large-Gap Quantum Spin Hall Insulators in Tin Films. *Phys. Rev. Lett.* **2013**, *111* (13), 136804.

(52) Sushkov, A. B.; Jenkins, G. S.; Schmadel, D. C.; Butch, N. P.; Paglione, J.; Drew, H. D. Far-Infrared Cyclotron Resonance and Faraday Effect in Bi 2Se3. *Phys. Rev. B: Condens. Matter Mater. Phys.* **2010**, *82* (12), 125110.

(53) Hada, M.; Norimatsu, K.; Tanaka, S.; Keskin, S.; Tsuruta, T.; Igarashi, K.; Ishikawa, T.; Kayanuma, Y.; Miller, R. J. D.; Onda, K.; et al. Bandgap Modulation in Photoexcited Topological Insulator Bi2Te3 via Atomic Displacements. *J. Chem. Phys.* **2016**, *145* (2), 024504.

(54) Wang, Y.; Luo, G.; Liu, J.; Sankar, R.; Wang, N. L.; Chou, F.; Fu, L.; Li, Z. Observation of Ultrahigh Mobility Surface States in a Topological Crystalline Insulator by Infrared Spectroscopy. *Nat. Commun.* **2017**, *8* (1), 366.

(55) Hohenberg, P.; Kohn, W. Inhomogeneous Electron Gas. *Phys. Rev.* **1964**, *136* (3B), B864−B871.

(56) Kohn, W.; Sham, L. J. Self-Consistent Equations Including Exchange and Correlation Effects. *Phys. Rev.* **1965**, *140* (4A), A1133−A1138.

(57) Kresse, G.; Furthmüller, J. Efficiency of Ab-Initio Total Energy Calculations for Metals and Semiconductors Using a Plane-Wave Basis Set. *Comput. Mater. Sci.* **1996**, *6* (1), 15−50.

(58) Kresse, G.; Furthmüller, J. Efficient Iterative Schemes for *Ab Initio* Total-Energy Calculations Using a Plane-Wave Basis Set. *Phys. Rev. B: Condens. Matter Mater. Phys.* **1996**, *54* (16), 11169−11186.

(59) Blöchl, P. E. Projector Augmented-Wave Method. *Phys. Rev. B: Condens. Matter Mater. Phys.* **1994**, *50* (24), 17953−17979.

(60) Mostofi, A. A.; Yates, J. R.; Pizzi, G.; Lee, Y. S.; Souza, I.; Vanderbilt, D.; Marzari, N. An Updated Version of Wannier90: A Tool for Obtaining Maximally-Localised Wannier Functions. *Comput. Phys. Commun.* **2014**, *185* (8), 2309−2310.

Supporting Information

to

Giant Photonic Response of Mexican-hat Topological Semiconductors for Mid-infrared to THz Applications

Haowei Xu[1], Jian Zhou[1], Hua Wang[1] and Ju Li[1,2]

[1] Department of Nuclear Science and Engineering, Massachusetts Institute of Technology, Cambridge, Massachusetts 02139, USA
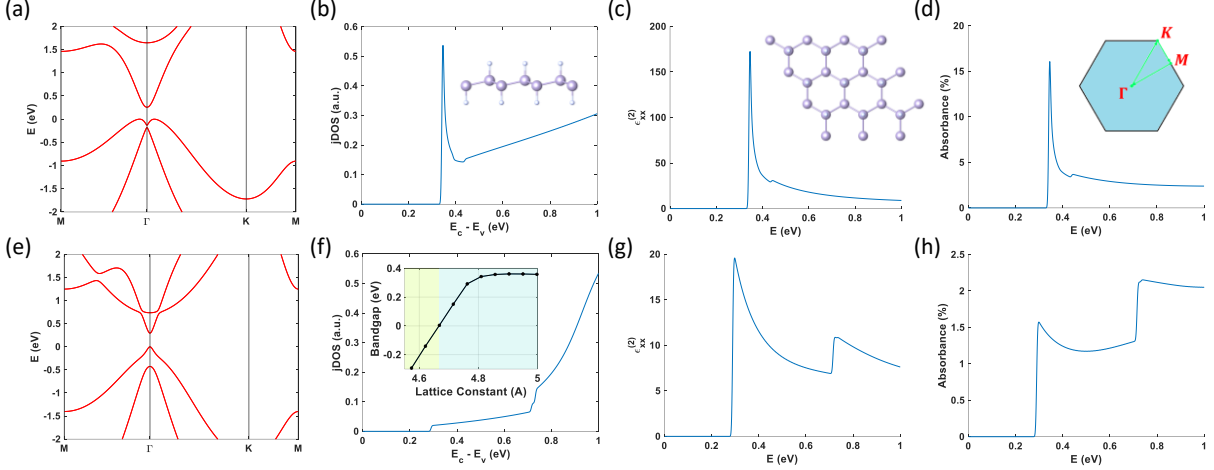
[2] Department of Materials Science and Engineering, Massachusetts Institute of Technology, Cambridge, Massachusetts 02139, USA

Table of Contents

I. 2D TIs with MHBS

As discussed in the main text, the optical response of 2D TIs with MHBS can be enhanced as well. Here we take monolayer SnF as an example.

Figure S1 The band structure and optical properties of 2D monolayer SnF. The four columns correspond to band structure, jDOS, imaginary part of dielectric response and gain, respectively. For the first row, the atomic structure of SnF has a 2% biaxial tensile strain, and it is a topological insulator with Mexican hat band structure. While for the second row, SnF has a -3% biaxial compressive strain, and is a normal insulator without band inverson. The dramatic improvement over optical properties induced by the band inversions and Mexican hat band structure can be seen by comparing two rows. Inset of (b, c): side and top view atomic structure of SnF. Inset of (d): first BZ of SnF. Inset of (f) band gap of monolayer SnF as a function of lattice constant a. The topologically non-trivial to trival phase transition happens at $a \approx 4.67$Å. A negative bandgap indicates that it is an inverted bandgap.

II. TIs without MHBS

TIs without Mexican hat band structure (MHBS) can already be good for THz laser and photodetector, while MHBS gives a further boost. In Figure 1 of the main text, we plotted $\mathcal{O}^{ij}(\boldsymbol{k}) = \left| A_{cv}^i(\boldsymbol{k}) A_{vc}^j(\boldsymbol{k}) \right|$, where $\boldsymbol{A}_{mn}(\boldsymbol{k}) = i \langle u_{m,\boldsymbol{k}} | \nabla_{\boldsymbol{k}} | u_{n,\boldsymbol{k}} \rangle$ is the Berry connection. One can see that $\mathcal{O}^{ij}(\boldsymbol{k})$ of TIs is larger than that of NIs by a factor of about 3 around the bandgap. Therefore, in general TIs should have stronger optical response than NIs, and can be better candidates for
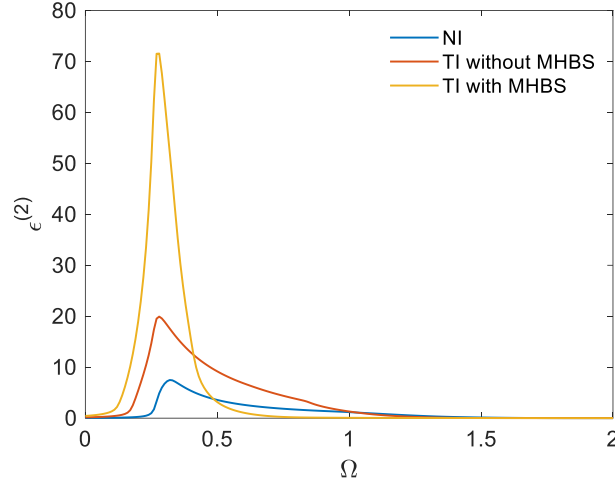
Figure S2 The imaginary part of the dielectric function of the model Hamiltonian as in Eq. (2) of the main text.

THz laser or photodetector even without MHBS. However, the MHBS provides a further boost in the optical response because $\mathcal{O}^{ij}(\mathbf{k})$ has a significant value over an extended region in the Brillouin zone, leading to a larger joint density of states.

In order to further illustrate this point, we calculate the dielectric response of the model Hamiltonian given by Eq. (2) in the main text, which is

$$H(\mathbf{k}) = \begin{bmatrix} M - B_+|k_+|^2 - B_z k_z^2 & A_+ k_+ + A_z k_z \\ A_+ k_+^* + A_z k_z & -(M - B_+|k_+|^2 - B_z k_z^2) \end{bmatrix}.$$

We use the same parameters as those used in Figure 1 of the main text, and the imaginary part of the dielectric function $\epsilon^{(2)}$ are plotted in the Figure S2. We can see that TI without MHBS already has an $\epsilon^{(2)}$ about 3 times larger than that of NI around the transition edge. For TI with MHBS, $\epsilon^{(2)}$ is boosted by another factor of 3~4.

## III. The Influence of Surface States

As discussed in the main text, the surface states of 3D TIs could affect the performance. However, the influence of the surface states should be relatively weak in the frequency range of interest, for two reasons:

1) These topological surfaces are actually *semi*-metallic, meaning that ideally there can be no free carriers on the surfaces. In practice, there could be free carriers from e.g., doping or thermal activation. But the density n of these free carriers should be smaller by several orders of magnitude than that in real metals. In real metals such as copper, n is usually on the order of 10^{28} m^{-3}, leading to huge dielectric response (both real and imaginary parts) from free-carrier contribution. Consequently, the absorption and reflection of light is very strong in real metals. On the other hand, for the surface states of TIs, n should be much smaller. Assuming $n = 10^{23}$ m^{-3}, the dielectric function is only on the order of 100 around the bulk bandgap, which cannot lead to very efficient absorption or reflection (in fact this is about 5 orders of magnitude smaller than that of copper). In addition, the plasma frequency of surface carriers with $n = 10^{23}$ m^{-3} is about 2 THz $\sim$ 8 meV. This frequency is well below the bandgap of the bulk material, which is the frequency range of interest. Therefore, one could expect that the reflection and absorption from the topological surface states are not very efficient.

2) The surface states only exist around the surface with a thickness on the order of 1 nm. However, upon reflection or absorption, the penetration depth of light needs to be on the order of $0.1 \sim 1$ μm (assuming a dielectric function $\sim$100 on the surfaces). Thus, the surface states are too thin to absorb or reflect the light strongly. For example, monolayer graphene, despite being a Dirac metal, allows 97.4% light transmission. For non-radiative recombination, the small thickness indicates small (joint) DOS, which depends linearly on the size. On the other hand, the bulk states, which are responsible for the high optical performance of TIs, exist in the entire bulk with much larger (joint) DOS. Since the transition rate of both the radiative and non-radiative processes should be (at least) linearly dependent on the (joint) DOS, one could expect that the non-radiative process on the surfaces is much slower than the radiative recombination in the bulk. Furthermore, when the laser is triggered, the radiative recombination would be dramatically accelerated by stimulated amplification, rendering the influence of the surface states even smaller.

These two factors combined, make the influence of the surface states relatively weak. There are experimental evidence for our points. For example, the total reflectivity of several TIs is found to

(a)

Absorbance (%) vs *ω (eV)*

(b)

$\epsilon^{(1)}$ vs *ω (eV)*
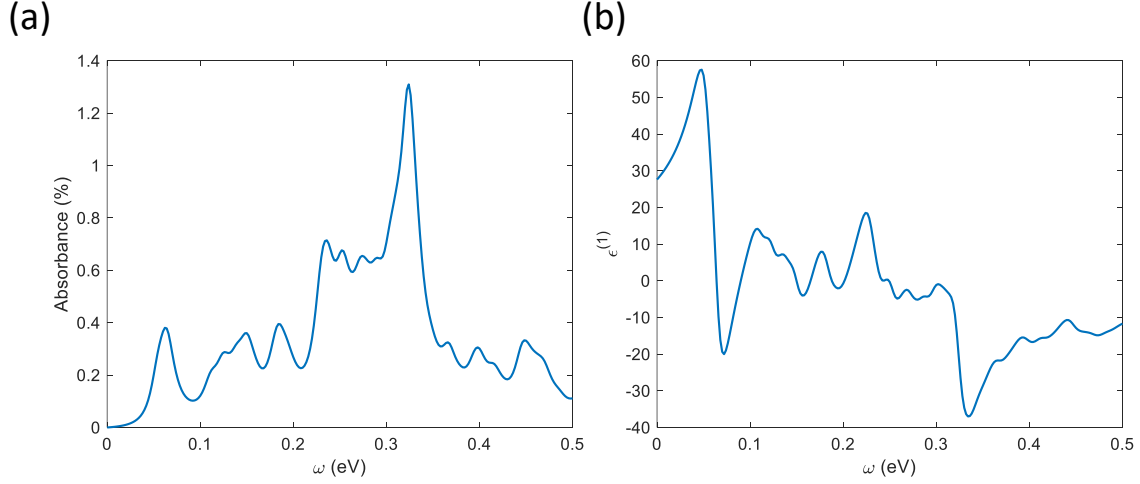
Figure S3 (a) The absorbance from the surface states of SnSe on the (100) surface. **(b)** The real part of the dielectric function of the (100) surface states of SnSe. A penetration depth of 1nm of the surface states in assumed in (b).

be about 0.5 near the bandgap of the bulk, which is the frequency region of interest[1–3]. Considering that the total reflectivity includes the contribution from the bulk, the pure reflectivity from the surface states should be even smaller.

We can also estimate the reflection and absorption of the surface states with a $\boldsymbol{k} \cdot \boldsymbol{p}$ model. In the detector mode, the absorption of MIR/FIR/THz photons from the surface states in fact provide yet another route for generating photocurrents that can be used for detection, which was proposed in Ref. [4]. For SnSe studied in this work, we adopt a $\boldsymbol{k} \cdot \boldsymbol{p}$ model with parameters suggested in Refs. [5,6] to calculate the surface absorbance and dielectric properties of the (100) face. The Hamiltonian is

$$H(\boldsymbol{k}) = \begin{bmatrix} m & -iv_{x+}k_x - v_{y+}k_y & -iv_{2x}k_x + v_{2y}k_y & -m' \\ iv_{x+}k_x - v_{y+}k_y & m & m' & -iv_{2x}k_x - v_{2y}k_y \\ iv_{2x}k_x + v_{2y}k_y & m' & -m & -iv_{x-}k_x - v_{y-}k_y \\ -m' & iv_{2x}k_x - v_{2y}k_y & iv_{x-}k_x - v_{y-}k_y & -m \end{bmatrix}$$

and the absorbance from the (100) surface states is shown in the Figure S3a, where one can see that within the frequency region of interest (~ 0.2 eV), the absorbance from surface states is less than ~ 1 %, indicating that the majority of the absorption should happen in the bulk.

Regarding the reflection by surface states, the reflection process is governed by the dielectric function, which is

$$\epsilon = \epsilon_f + \epsilon_e$$

The first term ϵ_f is the free carrier contribution, and can be expressed as $\epsilon_f(\omega) = \frac{4\pi i}{\omega\epsilon_0} \frac{ne^2\tau}{m(1-i\omega\tau)}$ from Drude model, where n is the density of free carriers, e is electron charge, m is the mass of the free carriers, while τ is the carrier lifetime. This term is usually huge in real 3D metals such copper due to extremely large n, and thus the penetration depth of light in these metals can be much smaller than its wavelength in vacuum. The second term ϵ_e comes from the interband transition of electrons as in Eq. (1) in the main text.

Different from real metals, the surface states of the TIs are actually *semi*-metallic. Therefore, ideally there should be no free carriers and $\epsilon_f = 0$. In reality n can be nonzero due to e.g., doping effect or thermal activations. But n should still be much smaller as compared with that in real metals. Assuming $n = 10^{23}$ m^{-3} and $\tau = 20$ ps, $\epsilon_f(\omega)$ is only on the order of 100 at $\omega = 1$ THz, which is not so big. The interband contribution ϵ_e from surface states is not very big as well. We calculate ϵ_e of the (100) surface of SnSe according to the $\boldsymbol{k} \cdot \boldsymbol{p}$ model above (Figure S3b). One can see the peak value is on the order of 100. Taking a total $\epsilon = 400$, the wavelength of MIR/FIR/THz photons on the surface of TIs should be $0.1 \sim 1\ \mu m$. Upon reflection, the penetration depth of the evanescent wave is usually comparable with the wavelength, and should be $0.1 \sim 1\ \mu m$ as well. This is much larger than the thickness of the surface states, which is on the order of 1 nm. Therefore, the reflection from the surface states can be kept weak as long as the free carrier density n is not too large.

IV. Results with HSE hybrid functionals

The DFT calculations with PBE functionals sometimes could yield wrong results regarding the topology of TIs. Thus we benchmark our main results (band structure, band topology and optical responses) of SnSe using hybrid functional Heyd, Scuseria, and Ernzerhof (HSE)[7,8] hybrid functional. The results are shown in Figure S4 below, where we can see that they are consistent with PBE results in Figure 2 of the main text.

Regarding Figure 3 in the main text, our exploration of TIs with MHBS is based upon an established database of topological materials[9,10]. This database is constructed with PBE functional,
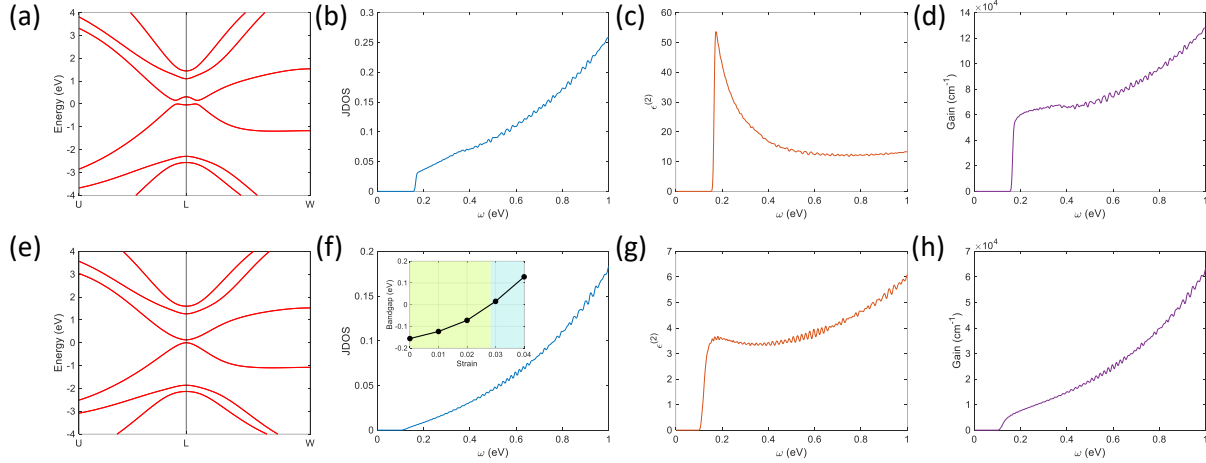
Figure S4 Band structure and optical properties of SnSe with HSE03+SOC. (a-d) correspond to a strain free SnSe, which is a TI with MHBS. The bandgap is around 0.16 eV. (e-h) correspond to SnSe with a 4% triaxial strain. In this case SnSe is a NI. The optical response of TI with MHBS is more than10 times stronger than of NI, consistent with the results in Figure 2 of the main text, which are obtained with PBE functional. Inset of (f) is the bandgap of SnSe as a function of strain. A negative bandgap indicates that it is inverted.

and a topological materials database with HSE functional would indeed be different. The construction of such an HSE database would be extremely expensive though.

Table R1 The band topology with HSE function of several materials in Fig. 3 of the main text whose gain are above $10^4 \ cm^{-1}$

Material	Topological Insulator	Mexican hat	Bandgap (eV)
Sb_2Te_2Se	Yes	Yes	0.22
PbSe	Yes	Yes	0.11
SnS	Yes	Yes	0.049
SnSe	Yes	Yes	0.16
SnTe	Yes	Yes	0.15
$TaThN_3$	No	No	/
HgS	No	No	/

Nevertheless, we focus on the band topology of materials in Figure 3 of the main text whose gain are above $10^4 \ cm^{-1}$. Among the seven materials, five are still TIs with MHBS when HSE functional is used. Table R1 indicate that HgS and $TaThN_3$ are not in the HSE database of TIs with

MHBS, but only in the PBE database. Actually, there should be other materials that are not present here and are only in the HSE database.

Of course, both PBE and HSE functionals can give wrong results regarding the band structure and band topology, and whether a material is TI with MHBS should have its own ground truth regardless of the functional used. But this would not hurt the main conclusion of the present work, that is, TIs with MHBS have enhanced optical responses.

References

(1)   Sushkov, A. B.; Jenkins, G. S.; Schmadel, D. C.; Butch, N. P.; Paglione, J.; Drew, H. D. Far-Infrared Cyclotron Resonance and Faraday Effect in Bi 2Se3. *Phys. Rev. B - Condens. Matter Mater. Phys.* **2010**, *82* (12), 125110.

(2)   Hada, M.; Norimatsu, K.; Tanaka, S.; Keskin, S.; Tsuruta, T.; Igarashi, K.; Ishikawa, T.; Kayanuma, Y.; Miller, R. J. D.; Onda, K.; et al. Bandgap Modulation in Photoexcited Topological Insulator Bi2Te3 via Atomic Displacements. *J. Chem. Phys.* **2016**, *145* (2), 024504.

(3)   Wang, Y.; Luo, G.; Liu, J.; Sankar, R.; Wang, N. L.; Chou, F.; Fu, L.; Li, Z. Observation of Ultrahigh Mobility Surface States in a Topological Crystalline Insulator by Infrared Spectroscopy. *Nat. Commun.* **2017**, *8* (1), 1–8.

(4)   Zhang, X.; Wang, J.; Zhang, S. C. Topological Insulators for High-Performance Terahertz to Infrared Applications. *Phys. Rev. B - Condens. Matter Mater. Phys.* **2010**, *82* (24), 245107.

(5)   Wang, Y. J.; Tsai, W. F.; Lin, H.; Xu, S. Y.; Neupane, M.; Hasan, M. Z.; Bansil, A. Nontrivial Spin Texture of the Coaxial Dirac Cones on the Surface of Topological Crystalline Insulator SnTe. *Phys. Rev. B - Condens. Matter Mater. Phys.* **2013**, *87* (23), 235317.

(6)   Liu, J.; Duan, W.; Fu, L. Two Types of Surface States in Topological Crystalline Insulators. *Phys. Rev. B - Condens. Matter Mater. Phys.* **2013**, *88* (24), 241303.

(7)   Heyd, J.; Scuseria, G. E.; Ernzerhof, M. Hybrid Functionals Based on a Screened Coulomb Potential. *J. Chem. Phys.* **2003**, *118* (18), 8207–8215.

(8)   Heyd, J.; Scuseria, G. E.; Ernzerhof, M. Erratum: "Hybrid Functionals Based on a Screened Coulomb Potential" [J. Chem. Phys. 118, 8207 (2003)]. *J. Chem. Phys.* **2006**, *124* (21), 219906.

(9)   Bradlyn, B.; Elcoro, L.; Cano, J.; Vergniory, M. G.; Wang, Z.; Felser, C.; Aroyo, M. I.; Bernevig,

B. A. Topological Quantum Chemistry. *Nature* **2017**, *547* (7663), 298–305.

(10)   Vergniory, M. G.; Elcoro, L.; Felser, C.; Regnault, N.; Bernevig, B. A.; Wang, Z. A Complete

Catalogue of High-Quality Topological Materials. *Nature* **2019**, *566* (7745), 480–485.